Journal of Molecular Structure 1317 (2024) 139115

Contents lists available at ScienceDirect

Journal of Molecular Structure

journal homepage: www.elsevier.com/locate/molstr

Effect of variation of substitution groups attached on benzoxazole ligands on relaxation dynamics of a family of nona-coordinate mononuclear dysprosium zero-field single-molecule magnets

Bianying Niu [a,1], Xuexue Li [a,1], Rajanikanta Rana [b], Jintao Zhang [a], Shirui Chen [a], Hongshan Ke [a,c,**], Lin Sun [d,*], Gang Xie [a], Sanping Chen [a,*], Gopalan Rajaraman [b,*]

[a] Key Laboratory of Synthetic and Natural Functional Molecule Chemistry of Ministry of Education, College of Chemistry and Materials Science, Northwest University, Xi'an 710127, PR China
[b] Department of Chemistry, Indian Institute of Technology Bombay, Powai, Mumbai 400076, India
[c] State Key Laboratory of Rare Earth Resource Utilization, Changchun Institute of Applied Chemistry, Chinese Academy of Sciences, Changchun 130022, PR China
[d] Henan Key Laboratory of Polyoxometalate Chemistry, Institute of Molecular and Crystal Engineering, College of Chemistry and Chemical Engineering, Henan University, Kaifeng 475004, PR China

ARTICLE INFO

Keywords:
Mononuclear
Dysprosium
Single-molecule magnets
Benzoxazole modification
Theoretical calculations

ABSTRACT

Taking advantage of modified substitution group strategy, the magneto-structural correlation of four nona-coordinate mononuclear dysprosium zero-field single-molecule magnets derived from benzoxazole ligands is established. Mixing of the corresponding benzoxazole ligands and dysprosium trifluoromethanesulfonate in the presence of methanol solvent yielded four nona-coordinate mononuclear dysprosium complexes **1**–**4** with the core molecular formula $Dy(L_{x\text{-}R})_3$ (R = F, **1**, x = 1; CN, **2**, x = 2; CF_3, **3**, x = 3 and $C(CH_3)_3$, **4**, x = 4). The coordination geometries of the dysprosium metal site with N_6O_3 donor atoms in **1**–**4** are all belong to spherical capped square antiprism (C_{4v}) and the detailed corresponding parameters are 1.509, 1.173, 1.412 and 1.377, respectively. The static and dynamic magnetic susceptibilities measurements were performed on **1**–**4**. They all display frequencies-dependent ac out-of-phase component signal peaks at different temperatures and zero external field, characteristic of single-molecule magnets behaviour. Variable-field magnetization measurements performed at 2 K confirm the magnetization blocking for **1**–**4** and reveal the presence of butterfly shape magnetic hysteresis. The experimental resulted effective energy barriers for magnetization reversal for **1**–**4** are 48.6, 102.2, 113.5, and 120.6 K, respectively. To understand the origin of variation observed, we have performed ab initio CASSCF/RASSI-SO/SINGLE_ANISO calculations on complexes **1**–**4**. The calculations reveal axial g-tensors within the ground KD state, aligning with experimental results, and contributing to the observed trend in barrier heights. The computed crystal field parameters show an increasing trend from **1** to **4**, indicating strengthening axial bonds, while non-axial CF parameters decrease. Steric hindrance from bulky ligands correlates with weakened equatorial bond strength, further contributing to higher barrier heights. Additionally, the LoProp charge on axial atoms strengthens the bonds in the order **1** → **2** → **3** → **4**, reaffirming the importance of strengthen axial bond and weakening equatorial bonds towards better performant SIMs. Our work demonstrates that ligand substituent group strategy applied on benzoxazoles can utilize to tune the magnetic anisotropy of nona-coordinate mononuclear dysprosium complexes.

* Corresponding authors.
** Corresponding author at: Key Laboratory of Synthetic and Natural Functional Molecule Chemistry of Ministry of Education, College of Chemistry and Materials Science, Northwest University, Xi'an 710127, PR China.
E-mail addresses: hske@nwu.edu.cn (H. Ke), sunlin@vip.henu.edu.cn (L. Sun), sanpingchen@nwu.edu.cn (S. Chen), rajaraman@chem.iitb.ac.in (G. Rajaraman).
[1] These authors contributed equally to this work.

https://doi.org/10.1016/j.molstruc.2024.139115
Received 30 April 2024; Received in revised form 8 June 2024; Accepted 23 June 2024
Available online 24 June 2024

1. Introduction

In 2003, the seminal work highlighted by Ishikawa related to the crystal structure and magnetic property of $[TbPc_2][N(C_4H_9)_4]$ sandwich double-decker compound ignited the research interest concerning to single-molecule magnets of f-block metal ions, where Pc represents the dianion form of phthalocyanine [1]. Since then, a plethora of lanthanide-based mononuclear single molecule magnets has been documented [2–10]. Meanwhile, the most utilized lanthanide metal ions are concentrated on heavy lanthanide cations such as Tb^{III}, Dy^{III} and Er^{III} due to their strong spin-orbital coupling and large magnetic anisotropy [11–16].

The factors that affected the magnetic anisotropy of dysprosium ion were various, including molecule encapsulation in metal-organic framework through host-guest interaction and single-wall carbon nanotube encapsulation [17,18], ancillary ligands coordinated with different charge densities [19], coordination atom replacement [20], the application of external electric field and pressure [21–24], light [25], macrocyclic ligand planar distortion [26], stereoelectronic effect [27], positional isomers [28], different non-coordinated anions in the secondary coordination sphere [29,30], coordinated anions nature [31], equatorial negative charge modulation [32], terminal substituent effect anchored on neutral Schiff-base ligands [33], single-crystal to single-crystal transformation [34,35], ligand substituents [36,37], polymorphism [38], different solvent molecules [39,40], second-sphere interactions [41], fluxionality [42], bond length [43], coordination environment variation [44,45]. Thus, the discrepancy in the relaxation dynamics of mononuclear dysprosium complexes can be reflected by the variation of the corresponding magnetic anisotropy.

Regarding the ligand substituents effects affect the magnetic anisotropy of mononuclear dysprosium complexes, several situations were illustrated by the previous published results. For instance, substitute one pyrrole nitrogen atom in the porphyrin core by oxygen and sulfur atoms demonstrated coordinating atom replacement strategy resulting in the enhancement of magnetic anisotropy and effective energy barrier [20]. Furthermore, modifying the non-coordinated atom or group in the secondary coordination sphere led to the changes of coordination geometry and magnetism [27]. The same non-coordinated atom or group anchored on the organic ligand with different positions dramatically demonstrated the influence of positional isomerism on magnetic properties [28]. The difference in the non-coordinated terminal substituent groups anchored on neutral Schiff-base ligands tuned the coordination geometries around the Dy^{III} ions and the resulting dynamic magnetic properties, which originates from different number of corresponding Schiff-base ligands ligated to the Dy^{III} centers [33]. These ligand substitution strategies covering the ligands varied from porphyrin derivatives [20], 2-amidinopyrimidine analogues [27], N,N'-bis (2-hydroxy-benzyl)-N,N'-bis(2-picolyl)ethylenediamine derivatives [28,36], Schiff-base [33,37], β-diketonate [40]. However, the ligand substituent effect of benzoxazoles has not been employed to the exploration of tuning the magnetic anisotropy of mononuclear dysprosium complexes.

Herein, we initially established the magneto-structural correlation of four nona-coordinate mononuclear dysprosium zero-field single-molecule magnets derived from benzoxazole ligands by means of ligand substituent group strategy. We present the syntheses, crystal structure analyses, magnetic properties and theoretical calculations of four nona-coordinate monomuclear dysprosium zero-field single-molecule magnets.

2. Experimental section

2.1. General procedures

All reactions and manipulations were performed under aerobic conditions. Unless stated otherwise, all materials were purchased from commercial sources without further purification. Dysprosium trifluoromethanesulfonate was acquired by dissolving dysprosium oxide in trifluoromethanesulfonic acid. The 8-hydroxyquinoline-2-carbaldehyde was synthesized by following the previously reported method [46]. 2-amino-4-(trifluoromethyl)phenol and 2-amino-4-cyanphenol were synthesized according to procedures published beforehand [47,48].

2.2. Synthesis of HL1, HL2, HL3 and HL4 ligands

The preparation and characterization of the Schiff base precursor (E)−2-(((4-fluoro-2-hydroxyphenyl)imino)methyl)quinolin-8-ol was described as follows: 2-amino-4-fluorophenyl (1.27 g, 10 mmol) was dissolved in 40 mL of toluene under stirring and heating at 108 °C and when the solution became clear, 8-hydroxyquinoline-2-carbaldehyde (1.73 g, 10 mmol) dissolved in 40 mL of toluene was slowly added dropwise. The reaction mixture was condensed and refluxed for 6 h under stirring and then subsequently cooled to room temperature. The final solution was stored in a freezer at −25 °C for two days to produce a dark brown solid, which was collected by suction filtration. The resultant solid was washed with cold toluene three times and dried under vacuum. Yield: 2.03 g, 72 %. ^{1}H NMR (400 MHz, d_6-DMSO, Fig. S1): δ 9.99 (s, 1H), 9.35 (s, 1H), 8.90 (s, 1H), 8.48 (d, 1H), 8.43 (d, 1H), 7.52 (t, 1H), 7.47 (dd, 1H), 7.26 (dd, 1H), 7.18 (dd, 1H), 7.01 (m, 1H), 6.96 (m, 1H).

(E)−2-(((4-fluoro-2-hydroxyphenyl)imino)methyl)quinolin-8-ol (2.82 g, 10 mmol) was dissolved in 60 mL of methanol under stirring at room temperature. When the solution became clear, then solid $AgNO_3$ (2.55 g, 15 mmol) was slowly added and the color of the mixture has become darker. The reaction progress was checked by thin layer chromatography (TLC). Upon the completion of this reaction, the solvent was evaporated to dryness and the black crude product was chromatographed on silica gel (200–300 mesh) with n-hexane and ethyl acetate (40:1–50:1, v/v) to give the pale pink solid product (2-(5-fluorobenzo[d]oxazol-2-yl)quinolin-8-ol) HL_1. Yield: 1.57 g, 56 %. ^{1}H NMR (400 MHz, d_6-DMSO, Fig. S2): δ 10.16 (s, 1H), 8.56 (d, 1H), 8.40 (d, 1H), 7.97 (m, 1H), 7.83 (dd, 1H), 7.57 (t, 1H), 7.52 (dd, 1H), 7.42 (m, 1H), 7.24 (dd, 1H).

The synthetic procedure of Schiff base ligand precursor (E)−3-hydroxy-4-(((8-hydroxyquinolin-2-yl)methylene)amino)benzonitrile was analogous to that of (E)−2-(((4-fluoro-2-hydroxyphenyl)imino)methyl) quinolin-8-ol, replacing 2-amino-4-fluorophenyl with 2-amino-4-cyanphenol (Fig. S3). The bright yellow solid product that formed was filtered, washed with cooled toluene three times and dried under vacuum. Yield: 2.43 g, 84 %.^{1}H NMR (400 MHz, d_6-DMSO, Fig. S4): δ 10.58 (s, 1H), 9.99 (s, 1H), 8.91 (s, 1H), 8.44 (m, 2H), 7.78 (d, 1H), 7.60 (dd, 1H), 7.54 (t, 1H), 7.49 (dd, 1H), 7.19 (dd, 1H), 7.09 (d, 1H).

The synthetic procedure of HL_2 was analogous to that of HL_1 except solid (diacetoxyiodo)benzene (3.22 g, 10 mmol) substituting solid $AgNO_3$ (2.55 g, 15 mmol), thus yielding the faint yellow solid product (2-(8-hydroxyquinolin-2-yl)benzo[d]oxazole-5-carbonitrile) HL_2. Yield: 1.41 g, 49 %. ^{1}H NMR (400 MHz, d_6-DMSO, Fig. S5): δ 10.19 (s, 1H), 8.56 (d, 2H), 8.43 (d, 1H), 8.14 (d, 1H), 8.02 (dd, 1H), 7.58 (t, 1H), 7.53 (d, 1H), 7.25 (dd, 1H).

The synthetic procedure of Schiff base (E)−2-(((2-hydroxy-4-(trifluoromethyl)phenyl)imino)methyl)quinolin-8-ol was analogous to that of (E)−2-(((4-fluoro-2-hydroxyphenyl)imino)methyl)quinolin-8-ol, replacing 2-amino-4-fluorophenyl with 2-amino-4-(trifluoromethyl) phenol (Fig. S6). The orange solid product that formed was filtered, washed with cooled toluene three times and dried under vacuum. Yield: 2.66 g, 80 %.

According to synthetic procedure described for HL_2, (2-(5-(trifluoromethyl)benzo[d]oxazol-2-yl)quinolin-8-ol) HL_3 was successfully prepared as pale pink solid product. Yield: 2.08 g, 63 %. ^{1}H NMR (400 MHz, d_6-DMSO, Fig. S7): δ 10.18 (s, 1H), 8.55 (d, 1H), 8.39 (d, 1H), 8.33 (s, 1H), 8.12 (d, 1H), 7.89 (m, 1H), 7.57 (t, 1H), 7.51 (m, 1H), 7.24 (m, 1H).

The Schiff base (E)−2-(((4-(tert-butyl)−2-hydroxyphenyl)imino) methyl)quinolin-8-ol was obtained following the procedure we mentioned above. The yellow solid product that formed was filtered, washed with cooled toluene three times and dried under vacuum. Yield: 2.40 g, 75 %. ^{1}H NMR (400 MHz, d_6-DMSO, Fig. S8): δ 9.94 (s, 1H), 9.17 (s, 1H), 8.97 (s, 1H), 8.49 (d, 1H), 8.42 (d, 1H), 7.51 (t, 1H), 7.46 (d, 1H), 7.32 (s, 1H), 7.18 (d, 1H), 7.16 (d, 1H), 6.90 (d, 1H), 1.30 (s, 9H).

The preparation of HL_4 was analogous to that for HL_1. Pure white solid product (2-(5-(tert-butyl)benzo[d]oxazol-2-yl)quinolin-8-ol) HL_4 was generated. Yield: 1.59 g, 50 %. ^{1}H NMR (400 MHz, d_6-DMSO, Fig. S9): δ 10.10 (s, 1H), 8.52 (d, 1H), 8.40 (d, 1H), 7.89 (d, 1H), 7.80 (d, 1H), 7.60 (d, 1H), 7.56 (t, 1H), 7.51 (d, 1H), 7.23 (d, 1H), 1.39 (s, 9H).

2.3. Syntheses of compounds 1–4

[Dy(L_1)$_3$] (1). HL_1 (0.042 g, 0.15 mmol) was dissolved in 15 mL of methanol, and a methanolic solution of triethylamine (0.20 mL, 0.20 mmol) was added to obtain a yellow clear solution. After 40 min of stirring, solid $Dy(CF_3SO_3)_3$ (0.030 g, 0.05 mmol) was added, and the red reaction mixture was stirred at room temperature for 3 h. Dark red block single crystals suitable for single-crystal structure determination were obtained after a week by slowly evaporating the solvent at room temperature. Yield 30.5 mg (61 %, based on the ligand). IR (KBr pellet, cm^{-1}): 3389(w), 3049(w), 1613(w), 1584(m), 1561(s), 1495(m), 1479 (m), 1460 (s), 1428(m), 1358(s), 1300(s), 1247(w), 1172(w), 1145(s), 1103(s), 955(m), 839(m), 813(m), 772(w), 736(m), 672(w), 612(w), 586(w), 546(w), 484(w), 469(w), 433(w). Elemental analysis calcd (%) for $DyC_{48}H_{24}O_6N_6F_3$ (Mr = 1000.23): C, 57.64; H, 2.42; N, 8.40. Found: C, 57.59; H, 2.38; N, 8.43.

[Dy(L_2)$_3$]·5CH_3OH (2). The procedure for the synthesis of **2** was followed a similar way to that of **1**, using HL_2 substitutes HL_1. Dark red block single crystals suitable for single-crystal structure determination were obtained after six days by slowly evaporating the solvent at room temperature. Yield 30 mg (51 %, based on the ligand). IR (KBr pellet, cm^{-1}): 3601(w), 3087(w), 2223(w), 1590(w), 1562(m), 1496(m), 1454 (s), 1428(s), 1349(s), 1302(s), 1284(w), 1261(m), 1148(w), 1105(m), 840(w), 819(w), 741(w), 489(w). Elemental analysis calcd (%) for $DyC_{56}H_{44}O_{11}N_9$ (Mr = 1181.50): C, 56.93; H, 3.75; N, 10.67. Found: C, 59.85; H, 3.71; N, 10.74.

[Dy(L_3)$_3$]·3CH_3OH (3). Complex **3** was prepared by following a similar way to that of **1**, using HL_3 instead of HL_1. Dark red block single crystals suitable for single-crystal structure characterization were obtained after a week by slowly evaporating the solvent at room temperature. Yield 27 mg (43 %, based on the ligand). IR (KBr pellet, cm^{-1}): 3424(m), 2363(m), 1569(w), 1496(w), 1462(s), 1361(s), 1326(s), 1272 (w), 1166(m), 1129(s), 1044(w), 935(w), 843(m), 744(w), 671(w). Elemental analysis calcd (%) for $DyC_{54}H_{36}O_9N_6F_9$ (Mr = 1246.39): C, 52.04; H, 2.91; N, 6.74. Found: C, 52.18; H, 2.93; N, 6.63.

[Dy(L_4)$_3$]·3CH_3OH (4). The preparation of **4** was adopted a similar way to that of **1**, using HL_4 in place of HL_1. Dark red block single crystals suitable for single-crystal structure analysis were obtained after a week by slowly evaporating the solvent at room temperature. Yield 33 mg (54.5 %, based on the ligand). IR (KBr pellet, cm^{-1}): 3437(m), 2963(w), 1599(s), 1570(s), 1456(s), 1427(m), 1360(s), 1298(s), 1144(m), 1102 (m), 839(w), 800(w), 743(m), 547(w), 485(w). Elemental analysis calcd (%) for $DyC_{63}H_{63}O_9N_6$ (Mr = 1210.69): C, 62.50; H, 5.25; N, 6.94. Found: C, 62.43; H, 5.32; N, 6.90.

2.4. Physical measurements

Elemental analyses for C, H, and N were performed with a VarioEL element analyzer. The FTIR spectra of as-synthesized complex **1**–**4** was recorded from KBr pellets in the range 4000–400 cm^{-1} on a VERTEX 70 Fourier transform infrared (FTIR) spectrophotometer. ^{1}H NMR spectra were recorded on a Bruker DRX-400 equipment at 400 MHz at 25 °C using d_6-DMSO as the solvent. Powder X-ray diffraction data (PXRD) were collected at 298 K on a Rigaku RU200 diffractometer operated at 60 kV under the scan rate of 5° min^{-1} and a step size of 0.3° in 2θ with a Cu Kα X-ray source (λ = 1.5406) Å. Thermogravimetric analysis (TGA) was carried out at a heating rate of 10 °C min^{-1} under constant nitrogen flow in the temperature range of 25–800 °C. Magnetic tests were performed from 2 to 300 K, using a Quantum Design MPMS XL-7 SQUID magnetometer staffed with a 5 T magnet. The diamagnetic correction of the complexes **1**–**4** was evaluated using Pascal's constants, and the magnetic data correction was performed on the diamagnetic contribution of the sample holder. For the magnetization measurements, the temperature was set between 2 and 5 K and the magnetic field intensity was set between 0 and 7 T. The in-phase and out-of-phase components of magnetic susceptibility of powder **1**–**4** were collected by alternating current susceptibility magnetic operations. Data acquisition was conducted by decreasing the temperature from 18 to 2 K for **1**, 22 to 2 K for **2**, 30 to 2 K for **3**, and 28 to 2 K for **4** under the condition of no external dc magnetic field and an oscillating frequency of 3.5 Oe with frequencies between 1 and 1000 Hz for **1** and **2** in addition 1–1500 Hz for **3**–**4**, respectively.

2.5. X-ray crystal structure determination

Single-crystal X-ray diffraction date were collected at 229 K for **1**, 170 K for **2**, 180 K for **3**, and 150 K for **4** on a Bruker Apex II CCD diffractometer with Ga Kα radiation (λ = 1.34139 Å) or Mo Kα radiation (λ = 0.71073 Å). The SAINT processing program was used for data reduction. The crystal structures were solved by direct methods and refined by full-matrix least squares methods based on F^2 by using the SHELXTL 2014 program [49]. All non-hydrogen atoms were refined anisotropically. Hydrogen atoms were introduced in calculated positions and refined as a fixed geometry on their parent atoms. The PLATON/SQUEEZE procedure was employed to complex **1, 2** and **4** to remove heavily disordered solvent molecules. A summary of the structural data and refinement details for complexes **1**–**4** is presented in Table S1. Correlated bond lengths (Å) of **1**–**4** are listed in Table S2. Selected geometrical parameters of complexes **1**–**4** are given in Table S4. CCDC deposition number 2,286,385–2,286,388 include related crystallographic files for this paper and these files can be downloaded free of charge via www.ccdc.cam.ac.uk/data_request/cif.

Electronic Supplementary Information (ESI) available: Crystallographic data and refinement details of **1**–**4** (Table S1), selected bond lengths for **1**–**4** (Table S2), intra-molecular contacts of **2**–**4** (Table S3), coordinate polyhedron analysis of **1**–**4** (Table S4), ^{1}H NMR spectrum of synthesized ligands (Figs. S1–S9), molecular structures and crystal packings of **1**–**4** (Figs. S10 and S11), powder X-ray diffraction (PXRD) patterns of **1**–**4** (Fig. S12), TGA curves of **1**–**4** (Fig. S13), magnetic properties and theoretical calculations performed on **1**–**4** (Figs. S14–19 and Tables S5–11).

2.6. Theoretical calculations details

The Gaussian16 package was employed to carry out all H-optimization using Density Functional Theory (DFT) calculations [50]. While conducting H optimizations, we substituted the central Dy^{III} ion with a diamagnetic Y^{III} ion, chosen due to its closely matched ionic radius. We employed the hybrid B3LYP functional, in conjunction with the SDD basis set and the corresponding ECP basis set for Y, alongside the 6–31G* basis set for the remaining atoms, throughout the optimization process.

Using MOLCAS 8.2 [51], ab initio calculations were conducted on trivalent lanthanide ions Dy utilizing single-crystal structural data. Relativistic effects were accounted for based on the Douglas-Kroll Hamiltonian [52]. The complete active space self-consistent field (CASSCF) method was employed to achieve spin-free eigenstates [53]. For Dy, the [ANO-RCC...8s7p5d3f2g1h] [54] basis set was utilized, while C atoms used the [ANO-RCC...3s2p] basis set, H atoms employed the [ANO-RCC...2 s] basis set, N atoms utilized the [ANO-RCC...3s2p1d]

basis set, and O atoms used the [ANO-RCC...3s2p1d] basis set. The CASSCF calculations included 9 electrons distributed across 7 4f orbitals of the Dy^{III} ion, with 21 roots computed in the configuration interaction (CI) procedure. Following the computation of excited states, all roots were mixed using RASSI-SO [55], incorporating spin-orbit coupling within the calculated space. Subsequently, the computed spin-orbit (SO) states were analyzed using the SINGLE_ANISO [56] program to compute the g tensors. Cholesky decomposition for 2-electron integrals was employed throughout the calculations [57]. Employing the SINGLE-ANISO computation, as implemented in MOLCAS 8.2, we derived the g tensor for both ground and excited states, along with magnetic susceptibility, crystal field parameters, and the orientation of the principal magnetic axes.

3. Results and discussion

3.1. Crystal structures of complexes 1–4

The mixture of the corresponding benzoxazole ligands and dysprosium trifluoromethanesulfonate in methanol solvent in the presence of triethylamine with molar ratio of 3:1:4 successfully generated four nona-coordinate mononuclear dysprosium complexes **1**–**4** with general molecular formula $Dy(L_{x\text{-}R})_3{\cdot}yCH_3OH$ (R = F, (**1**, x = 1 and y = 0); CN, (**2**, x = 2 and y = 5); CF_3, (**3**, x = 3 and y = 3) and $C(CH_3)_3$, (**4**, x = 4 and y = 3)). The tiny discrepancy of the ligands reflected by the variation of the substitution groups attached on the benzoxazole derivative ligands. Different types of substitution groups have been anchored to the benzoxazole moieties: **1**, L_1, R = F; **2**, L_2, R = CN; **3**, L_3, R = CF_3; and **4**, L_4, R = $C(CH_3)_3$ (Scheme S1).

Complex **1** crystallizes in the monoclinic C2/c space group with Z = 8. Both complexes **2** and **4** crystallize in the triclinic P1 space group with Z = 2, whereas complex **3** crystallizes in the monoclinic $P2_1/c$ space group with Z = 4. The solid-state molecular structures of them are shown in Figs. 1 and S10. Crystal data and structure refinements for **1**–**4** are tabulated in Table S1.

The asymmetric unit of each complex contains the entire molecule and is charge neutrality. The Dy^{III} metal center of all four complexes is nona-coordinate and its coordination composition includes the N_6O_3 donor atoms surrounded by three ligands. Each ligand provides two nitrogen atoms and one oxygen atom as the donor atoms coordinating to the dysprosium ion. The molecular structure pattern of **1**–**4** is almost identical in the core structure with the only minor difference originating from different substituent groups of the precursor aminophenol anchored on the benzoxazole ligands. Apart from this, different amounts of dissociative methanol solvent molecules existed in the structure.

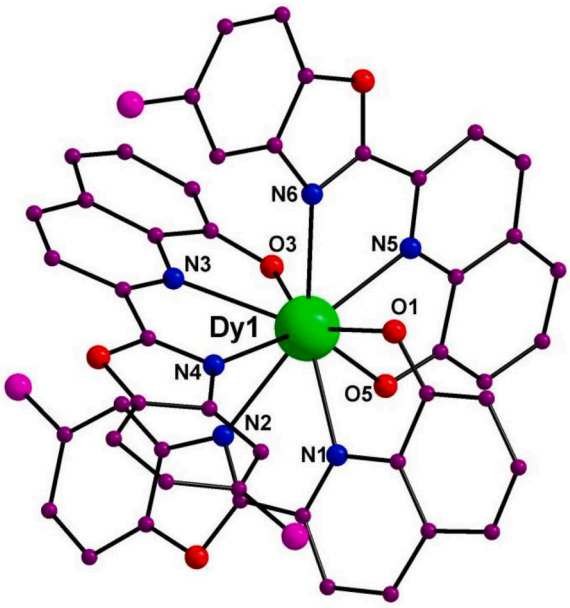

Fig. 1. The generalized molecular structures of neutral mononuclear nona-coordinate dysprosium complexes 1–4. Color codes: Dy, green; O, red; N, blue; C, violet. The pink color highlights the substitution group differences of the corresponding ligands in 1–4: 1, F; 2, CN; 3, CF_3; and 4, $C(CH_3)_3$. All hydrogen atoms and dissociative methanol molecules are deleted for clarity.

The average Dy-O bond lengths in **1**–**4** are 2.310(4), 2.314(4), 2.297 (5) and 2.329(2) Å as well the Dy-N bond lengths are 2.617(4), 2.616(5), 2.625(6), and 2.618(3) Å, respectively. The Dy-N bond lengths of **1**–**4** are 2.521(4), 2.709(4), 2.493(4), 2.613(5), 2.565(4) and 2.801(5) Å in **1**, 2.557(5), 2.794(5), 2.518(5), 2.645(5), 2.500(5) and 2.682(5) Å in **2**, 2.572(6), 2.822(6), 2.527(6), 2.677(6), 2.486(6) and 2.665(6) Å in **3** and 2.507(3), 2.633(3), 2.592(3), 2.830(3), 2.509(3) and 2.639(3) Å in **4**. The Dy-O bond distances in **1**–**4** corresponding to 2.309(4), 2.309(4) and 2.312(4) Å for **1**, 2.311(4), 2.339(4) and 2.291(4) Å for **2**, 2.294(5), 2.314(5) and 2.284(5) Å for **3**, and 2.345(2), 2.306(2) and 2.336(2) Å for **4**. The longest Dy-O bond distances in **1**–**4** corresponding to Dy1-O5, Dy1-O3, Dy1-O3, and Dy1-O1 are 2.312(4), 2.339(4), 2.314(5), and 2.314(5) Å, while the shortest Dy-O bond lengths are Dy1-O1, Dy1-O5, Dy1-O5, and Dy1-O5 with 2.309(4), 2.291(4), 2.284(5), and 2.306(2) Å, respectively. The longest Dy-N metal donor atom distances in **1**–**4** are Dy1-N6, Dy1-N2, Dy1-N2, and Dy1-N4 of 2.801(5), 2.794(5), 2.822(6), and 2.830(3) Å, whereas the shortest Dy-N bond distances in **1**–**4** related to Dy1-N3, Dy1-N5, Dy1-N5, and Dy1-N1 with detailed parameters of 2.493(4), 2.500(5), 2.486(6), and 2.507(3) Å. The detailed metal ligand donor atoms bond lengths information is shown in Table S2.

The crystal packing diagram for **1**–**4** is shown in Fig. S11. The stacking diagrams of four complexes are very similar as presented in Fig. S11.The following discussion of stacking mode in detail is confined to that of **1**.The molecular units are arranged regularly along the a-axis, forming 1D chains. These chains are arranged side by side, generating 2D layers parallel to the ab plane and the separation are resided by methanol solvent molecules. There are weak intra-molecular hydrogen bonding between mononuclear units and methanol molecules in **2**–**4** and the relevant intra-molecular contacts are listed in Table S3. No inter-molecular hydrogen bonding or π - π interactions exist between the mononuclear units in **1**–**4**. The shortest Dy···Dy distance is 9.975 Å, while the corresponding distances in **2**–**4** are 10.279, 9.986 and 9.406 Å.

In order to check the phase purity of **1**–**4**, PXRD tests were conducted, which showed that the experimental results match well with the theoretical simulation data (Fig. S12). The thermal stability of the four complexes was tested by thermogravimetric (TG) method (Fig. S13). They exhibited stability before 425 ℃, 400 ℃, 332 ℃ and 362 ℃, respectively, and the structures collapsed at higher temperatures. The coordination configurations of the four Dy^{III} metal centers were calculated with the aid of SHAPE software procedure [58]. The results of the coordination geometry of Dy^{III} are listed in Table S4. The coordination polyhedra of the Dy^{III} center sites all belong to spherical capped square antiprism (C_{4v}). The detailed corresponding parameters of **1**–**4** are 1.509, 1.173, 1.412 and 1.377, respectively.

3.2. Magnetic properties

The direct current (dc) magnetic susceptibility investigation was launched on crystalline powder solids in the 2–300 K temperature range under an applied external field of 1000 Oe for **1**–**4** and the results are illustrated in Fig. 2. At 300 K, the corresponding $\chi_M T$ values for **1**–**4** are 14.62, 14.06, 14.44, and 14.53 cm^3 K mol^{-1}, which are in accordance well with the theoretical value of 14.17 cm^3 K mol^{-1} expected for an isolated Dy^{III} ion ($^6H_{15/2}$, S = 5/2, L =5, g = 4/3, $\chi_M T$ = 14.17 cm^3 K mol^{-1}) with $^6H_{15/2}$ ground state doublets. With the temperature lowering, $\chi_M T$ keeps constant and reduces gradually, then decreases rapidly before 50 K to amounting to 11.89, 12.87, 13.18, and 8.89 cm^3 K mol^{-1} at 2 K. The decreasing behavior of $\chi_M T$ can be ascribed to the

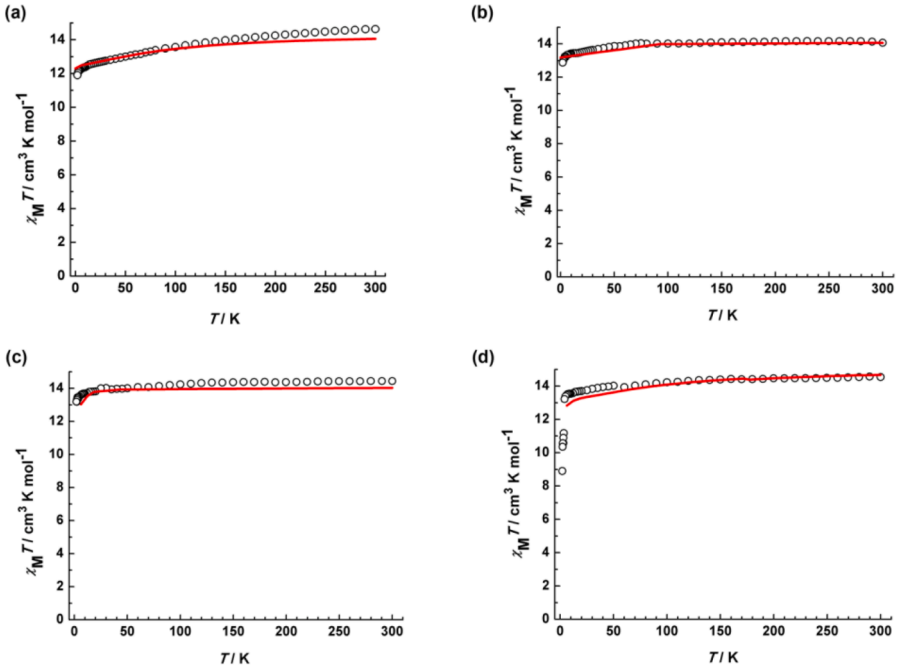

Fig. 2. χ_MT versus T plots measured from 2 to 300 K under 1000 Oe for complexes 1 (a), 2 (b), 3 (c) and 4 (d) with circle symbols and best fits derived from theoretical calculations (solid red lines).

influence factors originating from thermal depopulation of Stark sub-energy-level and considerable magnetic anisotropy.

The field dependence of isothermal magnetization was conducted on sweeping the field from 0 to 7 T with temperatures of 2, 3 and 5 K. A rapid increment is obvious for all four complexes in the low-field region. With the magnetic field increment, the magnetization enhances without approaching saturation at 7 T applied field. The maximum value of the magnetization for **1**–**4** reaches 5.36, 6.56, 5.91, and 6.40 μ_B at 2 K and 7 T (Fig. S14), which is lower than the theoretical saturated value of 10 μ_B for a free Dy^{III} ion. The non-superimpose nature of magnetization curves signifies the presence of considerable magnetic anisotropy and low-lying excited states. Magnetization hysteresis loop measurements at 2 K and applied fields varying from −5 to 5 T confirm the magnetization blocking for **1**–**4** (Figs. 3 and S15). No coercive fields observed under zero field at 2 K for **1**–**4** due to the presence of fast quantum tunneling of the magnetization [24,59]. The maximum opening for **1**–**4** appears

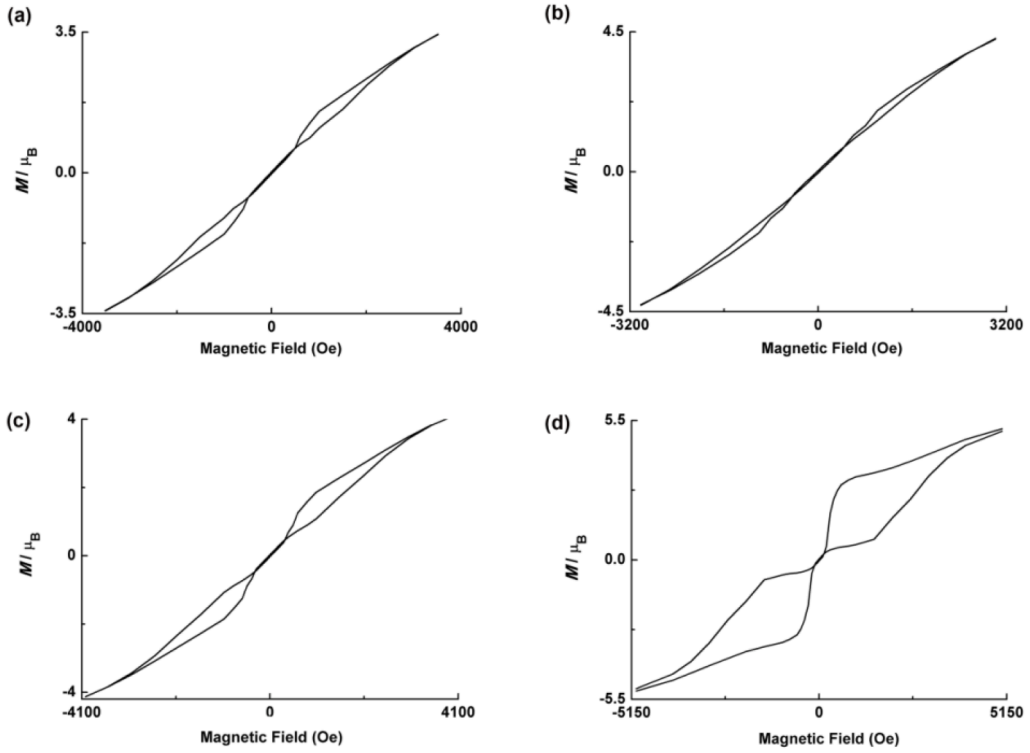

Fig. 3. Magnetization hysteresis loop plots at an average sweep of 50 Oe s^{-1} for 1 (a), 2 (b), 3 (c) and 4 (d) at 2 K.

below 2500, 2000, 2700, and 5200 Oe, thus the opening is widest in **4**. The magnetic hysteresis loops for **1**–**4** all feature S-shape and butterfly type. We can deduce from the analysis of the magnetization hysteresis loop that the prevalence of quantum tunneling of the magnetization is severe in **1** and **2** than that in **3** and **4**.

The frequency dependence of the dynamic ac magnetic susceptibility measurements were conducted for **1**–**4** under zero external field (Figs. 4 and S16). As can be seen, frequency dependent maximum signal peaks can be observed up to 18, 22, 30, and 28 K for **1**–**4**. The positions of the maximum signal peaks shifted to higher frequencies with temperature increment. χ_T, χ_S, τ and α parameters can be extracted from the simultaneously fitting the in-phase and out-of-phase magnetic susceptibilities experimental data by employing the generalized Debye model (Table S5) [60]. The resulting Cole-Cole plot is illustrated in Fig. S17 and constructed from the in-phase versus out-of-phase parts of magnetic susceptibilities. The parameters in **1**–**4** are in the range 0.08–0.14, 0.07–0.23, 0.02–0.16, and 0.02–0.22, indicating relatively narrow distribution of the relaxation times (τ). The ln τ versus T^{-1} plot is present in Fig. 5. Linear relationships can be observed at higher temperature regions 10–18, 12–22, 18–30, and 14–28 K and temperature-independent relationships below 6 K in addition curvature at intermediate temperatures for **1**–**4**. Such curves indicate the relaxation contributions from Orbach processes at higher temperatures and quantum tunneling of the magnetization at lower temperatures. The best fits to the experimental data was successful using the Eq. (1), in which τ_0 is the attempt

$$\tau^{-1} = {\tau_{QTM}}^{-1} + {\tau_0}^{-1} exp\left(-U_{eff} / \kappa_B T\right) \quad (1)$$

time, τ_{QTM}^{-1} is the rate for quantum tunneling and U_{eff} is the effective energy barrier for magnetization reversal. The resulting best fit afforded parameters for **1**–**4** are $U_{eff} = 48.6$ K, $\tau_0 = 2.06 \times 10^{-5}$ s, $\tau_{QTM} = 3.76 \times 10^{-4}$ s in **1**; $U_{eff} = 102.2$ K, $\tau_0 = 1.90 \times 10^{-6}$ s, $\tau_{QTM} = 4.22 \times 10^{-3}$ s in **2**; $U_{eff} = 113.5$ K, $\tau_0 = 2.74 \times 10^{-6}$ s, $\tau_{QTM} = 8.16 \times 10^{-4}$ s in **3**; and $U_{eff} = 120.6$ K, $\tau_0 = 2.18 \times 10^{-6}$ s, $\tau_{QTM} = 7.34 \times 10^{-3}$ s in **4**. The U_{eff} in **1**–**4** follows the trend **1 < 2 < 3 < 4**.

3.3. Theoretical calculations

Ab initio calculations on complexes **1**–**4** were performed with the MOLCAS 8.2 program of the CASSCF/RASSI-SO/SINGLE_ANISO type. Experimental findings indicate that the U_{eff} in **1**–**4** follows the trend **1 < 2 < 3 < 4**. The calculations have unveiled an axial series of g-tensors within the ground KD state, with the following values: $g_{zz} = 19.92$, $g_{yy} = 0.01$, $g_{xx} = 0.01$ for **1**, $g_{zz} = 19.93$, $g_{yy} = 0.01$, $g_{xx} = 0.01$ for **2**, $g_{zz} = 19.94$, $g_{yy} = 0.01$, $g_{xx} = 0.01$ for **3**, and $g_{zz} = 19.95$, $g_{yy} = 0.01$, $g_{xx} = 0.01$ for **4**. These findings align perfectly with the experimental results, demonstrating that the barrier height follows the order **1 < 2 < 3 < 4**, as the g_{zz} value is contingent on anisotropy shown in Table S6–9. A higher g_{zz} value contributes to a significant reduction in quantum tunneling (QTM) and thermally activated quantum tunneling (TA-QTM) in the magnetization relaxation mechanism, thereby increasing the barrier height. Also, in **1**–**4**, the ground state KDs predominantly exhibit pure m_J $|\pm 15/2>$ contributions, while the 1st excited KDs involve a mixture of m_J $|\pm 13/2>$ and other m_J levels, as detailed in Table S6–9. Consequently, the relaxation occurs in the 2nd KDs (Fig. S18). The calculated energy gap between the ground state KDs and the 1st excited KDs in **1**–**4** is 118.2, 150.0, 165.8, and 170.6 cm^{-1}, respectively. The transition moment between the ground KDs of **1**–**4** is 2.7×10^{-3}, 2.6×10^{-3}, 2.5×10^{-3}, and 9.0×10^{-4} μ_B, respectively. The transition moment within the 1st excited KDs in **1**–**4** is 0.09, 0.08, 0.08, and 0.037 μ_B, respectively.

To find out the origin of the increasing U_{cal} from **1 → 2 → 3 → 4**, we have estimated the crystal field parameters using the Hamiltonian $\widehat{\boldsymbol{H}}_{\boldsymbol{CF}} = \sum_{k=2,4,6} \sum_{q=-k}^{q=k} \boldsymbol{B}_k^q \widehat{\boldsymbol{O}}_k^q$ (here $\boldsymbol{B}_k^q$ is the crystal field parameter and $\widehat{\boldsymbol{O}}_k^q$ is the Stevens operator respectively). When we examine the axial crystal field (CF) parameters (B_k^0) across all complexes **1, 2, 3**, and **4**, we observe a clear trend of increasing values: **1 → 2 → 3 → 4**. Additionally, a noteworthy observation emerges when comparing the non-axial CF parameters, which exhibit a decreasing pattern in the order of **1 → 2 → 3 → 4**, shown in Table S10.

Examining from the anisotropy axis, it is evident that the axis lies

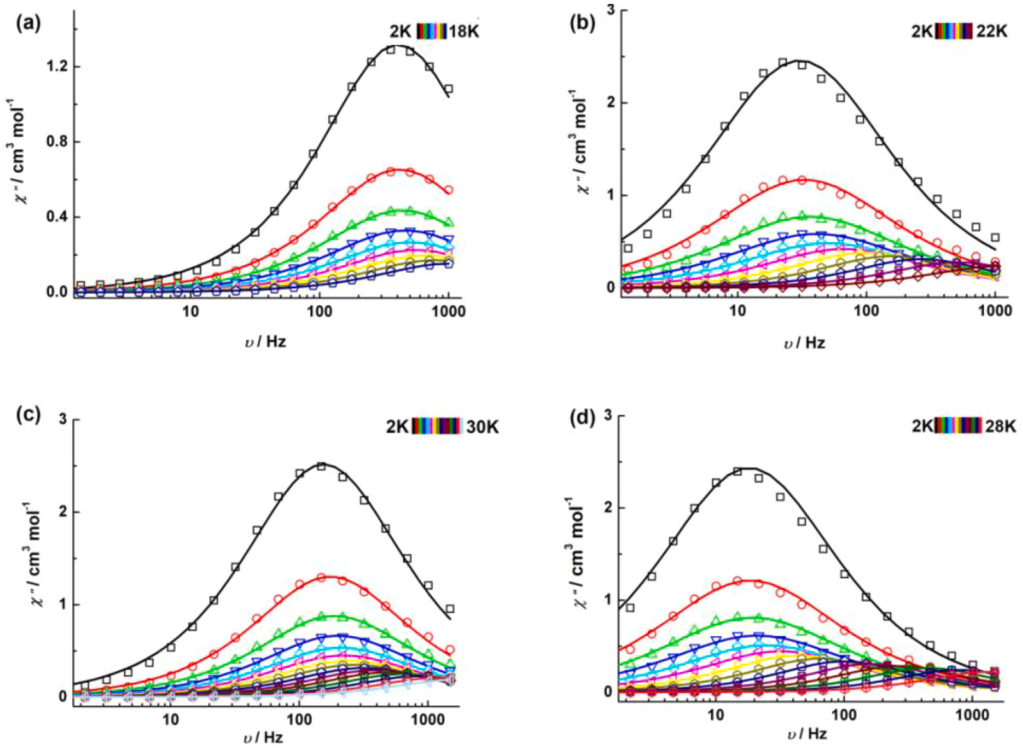

Fig. 4. Frequency dependence of the out-of-phase (χ_M'') ac magnetic susceptibility signals under zero external field for 1 (a), 2 (b), 3 (c) and 4 (d). Solid color lines represent best fits to the experimental data using the generalized Debye model.

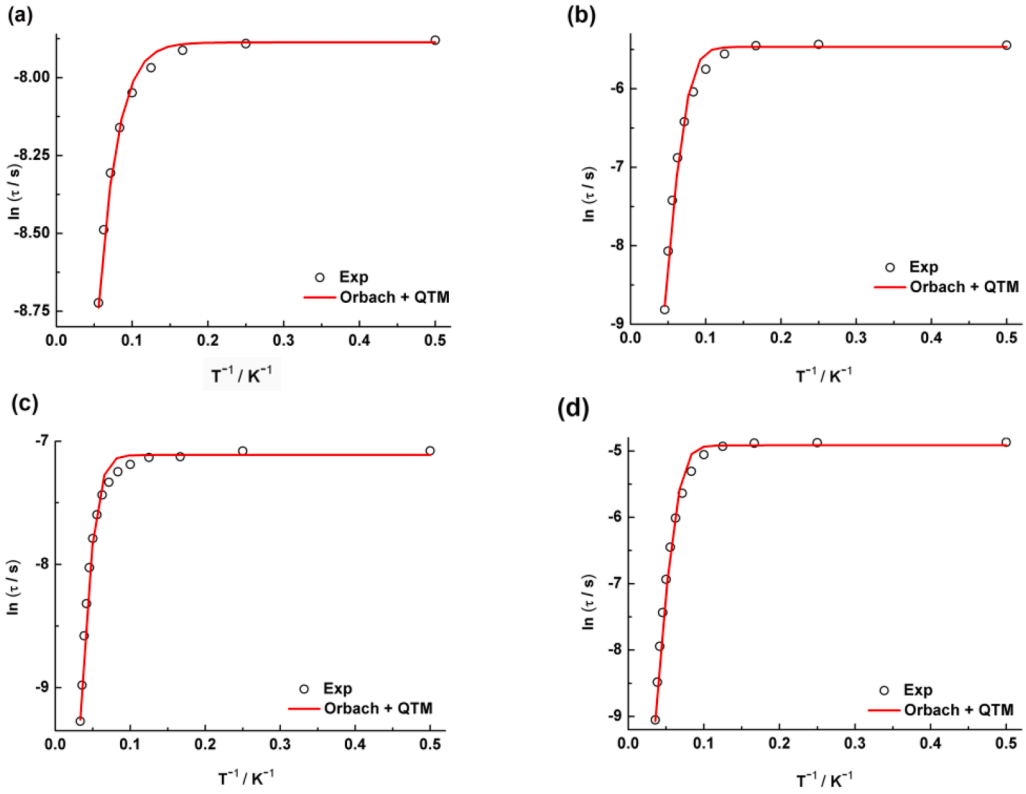

Fig. 5. Plot of ln τ versus inverse temperature for 1 (a), 2 (b), 3 (c) and 4 (d). The red solid lines correspond to the best fit as parameters indicated in the text.

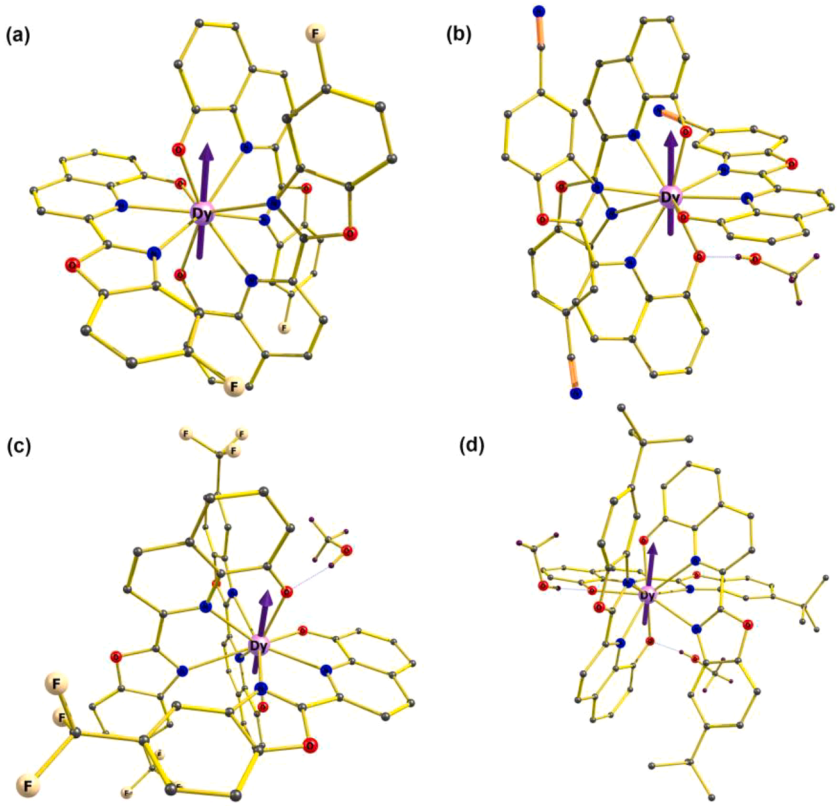

Fig. 6. Orientation of the magnetic anisotropy axis (g_{zz}) of 1 (a), 2 (b), 3 (c) and 4 (d). Dy, violet; O, red; N, blue; F, yellow; C, gray.

between the Dy-O and Dy-N bonds in complexes **1**–**4** shown in Fig. 6. When the strong bond aligns with the anisotropy axis, it results in higher anisotropy. Among these, the Dy-O bond is stronger than the Dy-N bond. Notably, in complex **1**, the Dy-O bond is slightly farther from the anisotropy axis compared to the other complexes, contributing to its lower barrier height. The beta spin density, reflecting the anisotropy of the complex, is directly linked to the barrier height. A comparison of beta spin density among **1** to **4** (Fig. S19) reveals that **1** has a less anisotropy, resulting in a lower barrier height compared to the others. Also, the ligands (F, CN, CF_3, and $C(CH_3)_3$) are attached to the equatorial positions. It is well-established that bulky ligands induce steric hindrance, weakening the bonds. In this case, the bulkiness of the ligands follows the order **1 < 2 < 3 < 4**, and with the same trend there is weakening of equatorial bond strength correspondingly, the barrier heights increases in the same order: **1 < 2 < 3 < 4**. This suggests a correlation between ligand bulkiness and the strength of equatorial bonds, contributing to higher barrier heights.

It is a recognized fact that a higher LoProp charge on the atom engaged in bonding with the metal center results in a stronger bond. In this context, it is evident that **1** exhibits the least negative LoProp charge on the axial atoms when compared to **2, 3**, and **4** shown in Table S11. This observation reinforces the idea that the strengthening of axial bonds in these complexes follows the order of **1 → 2 → 3 → 4**, providing further supporting evidence for this sequence.

4. Conclusions

Initial employment of modifying non-coordinated substitution group strategy to benzoxazole ligands, we successfully obtained four mononuclear dysprosium complexes. Solid-state single crystal structural characterization reveals that the coordination number of dysprosium ion in **1**–**4** is identical and is nona-coordinate. The N_6O_3 donor atoms surround the dysprosium centers leading to spherical capped square antiprism (C_{4v}) coordination geometry and the detailed corresponding parameters are 1.509, 1.173, 1.412 and 1.377, respectively. The static and dynamic magnetic susceptibilities measurements confirm that **1**–**4** behave as single-molecule magnets with effective energy barrier and butterfly shape magnetic hysteresis. The experimental deduced effective energy barriers for magnetization reversal for **1**–**4** are 48.6, 102.2, 113.5, and 120.6 K, respectively. Magnetization blocking can be observed for **1**–**4** at 2 K. The computations yielded axial g-tensor values (g_{zz}) for complexes **1** to **4**, consistent with experimental findings and establishing a barrier height order of **1 < 2 < 3 < 4**. Higher g_{zz} values mitigate quantum tunneling, augmenting barrier height and creating a gap between ground and first excited KD states. Crystal field analysis revealed ascending axial CF parameters and descending non-axial CF parameters from **1** to **4**. Additionally, the order of ligand bulkiness (**1 < 2 < 3 < 4**) correlated with the strength of equatorial bonds, influencing the respective barrier heights (**1 < 2 < 3 < 4**). Further support for the **1 → 2 → 3 → 4** barrier height sequence was derived from distances of axial bonds from the anisotropy axis, beta electron density plots, and LoProp charge analysis.

CRediT authorship contribution statement

Bianying Niu: Writing – original draft, Investigation, Data curation, Conceptualization. **Xuexue Li:** Writing – original draft, Investigation, Data curation. **Rajanikanta Rana:** Methodology, Formal analysis. **Jintao Zhang:** Validation. **Shirui Chen:** Validation. **Hongshan Ke:** Writing – review & editing, Writing – original draft, Project administration, Conceptualization. **Lin Sun:** Visualization. **Gang Xie:** Investigation. **Sanping Chen:** Investigation. **Gopalan Rajaraman:** Methodology, Formal analysis.

Declaration of competing interest

The authors declare that they have no known competing financial interests or personal relationships that could have appeared to influence the work reported in this paper.

Acknowledgments

This work has received financial supports from the National Natural Science Foundation of China (21601143 and 22203027), the Nature Science Foundation of Shaanxi Province (2021JM309) and the Open Funds of the State Key Laboratory of Rare Earth Resource of Changchun Institute of Applied Chemistry (RERU2021012), Science and Technology Innovation Team Program of Shaanxi Province (2022TD-32).

Supplementary materials

Supplementary material associated with this article can be found, in the online version, at doi:10.1016/j.molstruc.2024.139115.

References

[1] N. Ishikawa, M. Sugita, T. Ishikawa, S.Y. Koshihara, Y. Kaizu, Lanthanide double-decker complexes functioning as magnets at the single-molecule level, J. Am. Chem. Soc. 125 (2003) 8694–8695, https://doi.org/10.1021/ja029629n.
[2] M.A. Zykin, P.E. Kazin, M. Jansen, All-inorganic single-ion magnets in ceramic matrices, Chem. Eur. J. 26 (2020) 8834–8844, https://doi.org/10.1002/chem.202084161.
[3] W.B. Sun, P.F. Yan, S.D. Jiang, B.W. Wang, Y.Q. Zhang, H.F. Li, P. Chen, Z. M. Wang, S. Gao, High symmetry or low symmetry, that is the question high-performance Dy (III) single-ion magnets by electrostatic potential design, Chem. Sci. 7 (2016) 684–691, https://doi.org/10.1039/c5sc02986d.
[4] Z.H. Zhu, X.L. Li, S.T. Liu, J.K. Tang, External stimuli modulate the magnetic relaxation of lanthanide single-molecule magnets, Inorg. Chem. Front. 7 (2020) 3315–3326, https://doi.org/10.1039/d0qi00785d.
[5] A. Zabala-Lekuona, J.M. Seco, E. Colacio, Single-molecule magnets: from Mn12-ac to dysprosium metallocenes, a travel in time, Coord. Chem. Rev. 441 (2021) 213984, https://doi.org/10.1016/j.ccr.2021.213984.
[6] J.P. Sutter, V. Béreau, V. Jubault, K. Bretosh, C. Pichon, C. Duhayon, Magnetic anisotropy of transition metal and lanthanide ions in pentagonal bipyramidal geometry, Chem. Soc. Rev. 51 (2022) 3280–3313, https://doi.org/10.1039/d2cs00028h.
[7] Y.C. Chen, M.L. Tong, Single-molecule magnets: beyond a single lanthanide ion: the art of coupling, Chem. Sci. 13 (2022) 8716–8726, https://doi.org/10.1039/d2sc01532c.
[8] Y. Gil, A. Castro-Alvarez, P. Fuentealba, E. Spodine, D. Aravena, Lanthanide SMMs based on belt macrocycles: recent advances and general trends, Chem. Eur. J. 28 (2022) e202200336, https://doi.org/10.1002/chem.202200336.
[9] V.S. Parmar, D.P. Mills, R.E.P. Winpenny, Mononuclear dysprosium alkoxide and aryloxide single-molecule magnets, Chem. Eur. J. 27 (2021) 7625–7645, https://doi.org/10.1002/chem.202100085.
[10] Y.L. Li, H.L. Wang, Z.H. Zhu, F.P. Liang, H.H. Zou, Recent advances in the structural design and regulation of lanthanide clusters: formation and self-assemble mechanisms, Coord. Chem. Rev. 493 (2023) 215322, https://doi.org/10.1016/j.ccr.2023.215322.
[11] S. De, A. Mondal, Z.Y. Ruan, M.L. Tong, R.A. Layfield, Dynamics magnetic properties of germole-ligated lanthanide sandwich complexes, Chem. Eur. J. 29 (2023) e202300567, https://doi.org/10.1002/chem.202300567.
[12] Z.H. Zhu, J.K. Tang, Lanthanide single-molecule magnets with high anisotropy barrier: where to from here? Natl. Sci. Rev. 9 (2022) nwac194, https://doi.org/10.1093/nsr/nwac194.
[13] P.B. Jin, K.X. Yu, Q.C. Luo, Y.Y. Liu, Y.Q. Zhai, Y.Z. Zheng, Tetraanionic arachno-carboranyl ligand imparts strong axiality to terbium(III) single-moleculemagnets, Angew. Chem. Int. Ed. 61 (2022) e202203285, https://doi.org/10.1002/anie.202203285.
[14] F.S. Guo, B.M. Day, Y.C. Chen, M.L. Tong, A. Mansikkamäki, R.A. Layfield, Magnetic hysteresis up to 80 K in a dysprosium metallocene single molecule magnet, Science 362 (2018) 1400–1403, https://doi.org/10.1126/science.aav0652.
[15] S.K. Gupta, R. Murugavel, Enriching lanthanide single-ion magnetism through symmetry and axiality, Chem. Commun. 54 (2018) 3685–3696, https://doi.org/10.1039/c7cc09956h.
[16] S.K. Singh, B. Pandey, G. Velmurugan, G. Rajaraman, Key role of higher order symmetry and electrostatic ligand field design in the magnetic relaxation of low-coordinate Er(III) complexes, Dalton Trans. 46 (2017) 11913–11924, https://doi.org/10.1039/c6dt03568j.
[17] Y.J. Li, T.S. Wang, H.B. Meng, C. Zhao, M.Z. Nie, L. Jiang, C.R. Wang, Controlling the magnetic properties of dysprosium metallofullerene within metal-organic

frameworks, Dalton Trans. 45 (2016) 19226–19229, https://doi.org/10.1039/c6dt04180a.
[18] R. Nabi, R.K. Tiwari, G. Rajaraman, In silico strategy to boost stability, axiality, and barrier heights in dysprocenium SIMs via SWCNT encapsulation, Chem. Commun. 57 (2021) 11350–11353, https://doi.org/10.1039/d1cc03434k.
[19] K.S. Lim, J.J. Baldoví, W.R. Lee, J.H. Song, S.W. Yoon, B.J. Suh, E. Coronado, A. Gaita-Ariño, C.S. Hong, Switching of slow magnetic relaxation dynamics in mononuclear dysprosium (III) compounds with charge density, Inorg. Chem. 55 (2016) 5398–5404, https://doi.org/10.1021/acs.inorgchem.6b00410.
[20] W. Cao, C. Gao, Y.Q. Zhang, D.D. Qi, T. Liu, K. Wang, C.Y. Duan, S. Gao, J.Z. Jiang, Rational enhancement of the energy barrier of bis tetrapyrrole dysprosium SMMs via replacing atom of porphyrin core, Chem. Sci. 6 (2015) 5947–5954, https://doi.org/10.1039/c5sc02314a.
[21] A. Sarkar, G. Rajaraman, Modulating magnetic anisotropy in Ln (III) single-ion magnets using an external electric field, Chem. Sci. 11 (2020) 10324–10330, https://doi.org/10.1039/d0sc03982a.
[22] M. Briganti, F. Tottí, Magnetic anisotropy on demand exploiting high-pressure as remote control: an ab initio proof of concept, Dalton Trans. 50 (2021) 10621–10628, https://doi.org/10.1039/d1dt01719e.
[23] V.S. Parmar, A.M. Thiel, R. Nabi, G.K. Gransbury, M.S. Norre, P. Evans, S. C. Corner, J.M. Skelton, N.F. Chilton, D.P. Mills, Overgaard, Influence of pressure on a dysprosocenium single-molecule magnet, Chem. Commun. 59 (2023) 2656–2659, https://doi.org/10.1039/d2cc06722f.
[24] F. Pointillart, J.F. Gonzalez, H. Douib, V. Montigaud, C.J. McMonagle, B. L. Guennic, O. Cador, D. Pinkowicz, M.R. Probert, Reversible pressure-magnetic modulation in a tetrathiafulvalene-based dyad piezochromic dysprosium single-molecule magnet, Chem. Eur. J. 29 (2023) e202300445, https://doi.org/10.1002/chem.202300445.
[25] X.D. Huang, G.H. Wen, S.S. Bao, J.G. Jia, L.M. Zheng, Thermo- and light-triggered reversible interconversion of dysprosium-anthracene complexes and their responsive optical, magnetic and dielectric properties, Chem. Sci. 12 (2021) 929–937, https://doi.org/10.1039/d0sc04851h.
[26] Y. Gil, P. Fuentealba, A. Vega, E. Spodine, D. Aravena, Control of magnetic anisotropy by macrocyclic ligand distortion in a family of DyIII and ErIII single molecule magnets, Dalton Trans. 49 (2020) 17709–17718, https://doi.org/10.1039/d0dt03370g.
[27] A.A. Kitos, D.A. Gálico, N. Mavragani, R. Castaneda, J.O. Moilanen, J.L. Brusso, M. Murugesu, Probing optical and magnetic properties via subtle stereoelectronic effects in mononuclear Dy^{III}-complexes, Chem. Commun. 57 (2021) 7818–7821, https://doi.org/10.1039/d1cc02407h.
[28] Y.B. Dong, L. Zhu, B. Yin, X.R. Zhu, D.F. Li, Regulating the magnetic properties of seven coordinated Dy (III) singleion magnets through the effect of positional isomers on axial crystal-field, Dalton Trans. 50 (2021) 17328–17337, https://doi.org/10.1039/d1dt02925h.
[29] S.K. Gupta, S. Dey, T. Rajeshkumar, G. Rajaraman, R. Murugavel, Deciphering the role of anions and secondary coordination sphere in tuning anisotropy in Dy (III) air-stable D_{5h} SIMs, Chem. Eur. J. 28 (2022) e202103585, https://doi.org/10.1002/chem.202103585.
[30] J.F. Wu, O. Cador, X.L. Li, L. Zhao, B.L. Guennic, J.K. Tang, Axial ligand field in D_{4d} coordination symmetry: magnetic relaxation of Dy SMMs perturbed by counteranions, Inorg. Chem. 56 (2017) 11211–11219, https://doi.org/10.1021/acs.inorgchem.7b01582.
[31] J. Long, D.M. Lyubov, T.V. Mahrova, A.V. Cherkasov, G.K. Fukin, Y. Guari, J. Larionov, A.A. Trifonov, Synthesis, structure and magnetic properties of tris (pyrazolyl)methane lanthanide complexes: effect of the anion on the slow relaxation of magnetization, Dalton Trans. 47 (2018) 5153–5156, https://doi.org/10.1039/c8dt00458g.
[32] X.W. Cai, Z.J. Cheng, Y.Y. Wu, R. Jing, S.Q. Tian, L. Chen, Z.Y. Li, Y.Q. Zhang, H. H. Cui, A.H. Yuan, Tuning the equatorial negative charge in hexagonal bipyramidal dysprosium (III) single-ion magnets to improve the magnetic behavior, Inorg. Chem. 61 (2022) 3664–3673, https://doi.org/10.1021/acs.inorgchem.1c03775.
[33] H. Yang, S.S. Liu, Y.S. Meng, Y.Q. Zhang, L. Pu, X.C. Wang, S.J. Lin, Four mononuclear dysprosium complexes with neutral Schiff-base ligands: syntheses, crystal structures and slow magnetic relaxation behavior, Dalton Trans. 51 (2022) 1415–1422, https://doi.org/10.1039/d1dt03701c.
[34] J. Xi, P.P. Cen, Y. Guo, Y.Z. Li, Y.Y. Qin, Y.Q. Zhang, W.M. Song, X.Y. Liu, Reversible on-off switching of Dy (III) single-molecule magnets via single-crystal-to-single-crystal transformation, Dalton Trans. 51 (2022) 6707–6717, https://doi.org/10.1039/d2dt00501h.
[35] X.D. Huang, X.F. Ma, L.M. Zheng, Photo-responsive single-molecule magnet showing 0D to 1D single-crystal-to-single-crystal structural transition and hysteresis modulation, Angew. Chem. Int. Ed. 62 (2023) e202300088, https://doi.org/10.1002/anie.202300088.
[36] M.M. Wang, Y. Guo, Z.S. Han, X. Cheng, Y.Q. Zhang, W. Shi, P. Cheng, Impact of ligand substituents on the magnetization dynamics of mononuclear Dy^{III} single-molecule magnets, Inorg. Chem. 61 (2022) 9785–9791, https://doi.org/10.1021/acs.inorgchem.2c01299.
[37] K. Pramanik, Z. Jagličić, R. Herchel, P. Brandão, N.C. Jana, A. Panja, Combined experimental and theoretical studies on a series of mononuclear LnIII single-molecule magnets: dramatic influence of remote substitution on the magnetic dynamics in Dy analogues, Dalton Trans. 52 (2023) 1241–1256, https://doi.org/10.1039/d2dt03354b.
[38] X.F. Ma, Y. Guo, X.D. Huang, G.H. Wen, S.S. Bao, Y.Q. Zhang, L.M. Zheng, Polymorphism modulates photoluminescence and magnetic dynamics of mononuclear dysprosium-anthracene complexes, Dalton Trans. 51 (2022) 12026–12030, https://doi.org/10.1039/d2dt01710e.
[39] H.Q. Li, G.L. Wang, Y.C. Sun, Y.Q. Zhang, X.Y. Wang, Solvent modification of the structures and magnetic properties of a series of dysprosium (III) single-molecule magnets, Inorg. Chem. 61 (2022) 17537–17549, https://doi.org/10.1021/acs.inorgchem.2c02513.
[40] S. Zhang, N. Shen, J.W. Zhang, F. Xu, J. Zhang, J.M. Tang, D.W. Hu, B. Yin, S. P. Chen, Solvent responses and substituent effects upon magnetic properties of mononuclear Dy^{III} compounds, Dalton Trans. 50 (2021) 624–637, https://doi.org/10.1039/d0dt03477k.
[41] Y. Gil, L. Llanos, P. Cancino, P. Fuentealba, A. Vega, E. Spodine, D. Aravena, Effect of second-sphere interactions on the magnetic anisotropy of lanthanide single-molecule magnets: electrostatic interactions and supramolecular contacts, J. Phys. Chem. C 124 (2020) 5308–5320, https://doi.org/10.1021/acs.jpcc.9b09234.
[42] A. Swain, R.K. Tiwari, M. Khatua, G. Rajaraman, Fluxionality modulating the magnetic anisotropy in lanthanoarene $[(\eta C_nR_n)_2Ln(II/III)](n = 4\text{-}8)$ single-ion magnets, Inorg. Chem. 62 (2023) 9552–9562, https://doi.org/10.1021/acs.inorgchem.3c00956.
[43] Y. Li, Y. You, P. Zhao, Z.Y. Liu, Y.Q. Zhang, E.C. Yang, X.J. Zhao, Enhancing the magnetic anisotropy in low-symmetry Dy-based complexes by tuning the bond length, Inorg. Chem. 60 (2021) 11419–11428, https://doi.org/10.1021/acs.inorgchem.1c01437.
[44] A.K. Mondal, S. Goswami, S. Konar, Influence of the coordination environment on slow magnetic relaxation and photoluminescence behavior in two mononuclear dysprosium (III) based single molecule magnets, Dalton Trans. 44 (2015) 5086–5094, https://doi.org/10.1039/c4dt03620d.
[45] S. Yu, Z.L. Chen, H.C. Hu, B. Li, Y.N. Liang, D.C. Liu, H.H. Zou, D. Yao, F.P. Liang, Two mononuclear dysprosium (III) complexes with their slow magnetic relaxation behaviors tuned by coordination geometry, Dalton Trans. 48 (2019) 16679–16686, https://doi.org/10.1039/c9dt03253c.
[46] M.Y. Wu, G. Esteban, S. Brogi, M. Shionoya, L. Wang, G. Campiani, M. Unzeta, T. Inokuchi, S. Butini, J. Marco-Contelles, Donepezil-like multifunctional agents: design, synthesis, molecular modeling and biological evaluation, Eur. J. Med. Chem. 121 (2016) 864–879, https://doi.org/10.1016/j.ejmech.2015.10.001.
[47] K. Oshimoto, H. Tsuji, M. Kawatsura, Synthesis of benzoxazoles via the copper-catalyzed hydroamination of alkynones with 2-aminophenols, Org. Biomol. Chem. 17 (2019) 4225–4229, https://doi.org/10.1039/c9ob00572b.
[48] L. Ptiček, L. Hok, P. Grbčić, F. Topić, M. Cetina, K. Rissanen, S.K. Pavelić, R. Vianello, L. Racané, Amidino substituted 2-aminophenols: biologically important building blocks for the amidino-functionalization of 2-substituted benzoxazoles, Org. Biomol. Chem. 19 (2021) 2784–2793, https://doi.org/10.1039/d1ob00235j.
[49] G.M. Sheldrick, SHELXT-Integrated space-group and crystal-structure determination, Acta Crystallogr. Sect. A 71 (2015) 3–8, https://doi.org/10.1107/s2053273314026370.
[50] P.J. Stephens, F.J. Devlin, C.F. Chabalowski, M.J. Frisch, Ab initio calculation of vibrational absorption and circular dichroism spectra using density functional force fields, J. Phys. Chem. 98 (1994) 11623–11627, https://doi.org/10.1021/j100096a001.
[51] F. Aquilante, T.B. Pedersen, V. Veryazov, R. Lindh, MOLCAS-a software for multiconfigurational quantum chemistry calculations, WIREs Comput. Mol. Sci. 3 (2013) 143–149, https://doi.org/10.1002/wcms.1117.
[52] B.A. Heb, C.M. Marian, U. Wahlgren, O. Gropen, A mean-field spin-orbit method applicable to correlated wavefunctions, Chem. Phys. Lett. 251 (1996) 365–371, https://doi.org/10.1016/0009-2614(96)00119-4.
[53] B.O. Roos, P.Å. Malmqvist, Relativistic quantum chemistry: the multiconfigurational approach, Phys. Chem. Chem. Phys. 6 (2004) 2919–2927, https://doi.org/10.1039/b401472n.
[54] B.O. Roos, R. Lindh, P.Å. Malmqvist, V. Veryazov, P.O. Widmark, A.C. Borin, New relativistic atomic natural orbital basis sets for lanthanide atoms with applications to the Ce diatom and LuF_3, J. Phys. Chem. A 112 (2008) 11431–11435, https://doi.org/10.1021/jp803213j.
[55] P.Å. Malmqvist, B.O. Roos, B. Schimmelpfennig, The restricted active space (RAS) state interaction approach with spin-orbit coupling, Chem. Phys. Lett. 357 (2002) 230–240, https://doi.org/10.1016/s0009-2614(02)00498-0.
[56] L.F. Chibotaru, L. Ungur, Ab initio calculation of anisotropic magnetic properties of complexes. I. unique definition of pseudospin Hamiltonians and their derivation, J. Chem. Phys. 137 (2012) 064112, https://doi.org/10.1063/1.4739763.
[57] H. Koch, A. Sanchez de Merás, T.B. Pedersen, Reduced scaling in electronic structure calculations using Cholesky decompositons, J. Chem. Phys. 118 (2003) 9481–9484, https://doi.org/10.1063/1.1578621.
[58] A. Ruiz-Martínez, D. Casanova, S. Alvarez, Polyhedral structures with an odd number of vertices: nine-coordinate metal compounds, Chem. Eur. J. 14 (2008) 1291–1303, https://doi.org/10.1002/chem.200701137.
[59] C.G.T. Price, A. Mondal, J.P. Durrant, J.K. Tang, R.A. Layfield, Structural and magnetization dynamics of borohydride-bridged rare-earth metallocenium cations, Inorg. Chem. 62 (2023) 9924–9933, https://doi.org/10.1021/acs.inorgchem.3c01038.
[60] S.M.J. Aubin, Z.M. Sun, L. Pardi, J. Krzystek, K. Folting, L.C. Brunel, A. L. Rheingold, G. Christou, D.N. Hendrickson, Reduced anionic Mn_{12} molecules with half-integer ground states as single-molecule magnets, Inorg. Chem. 38 (1999) 5329–5340, https://doi.org/10.1021/ic990613g.